Very long-periodic pulsations detected simultaneously in a white-light flare and sunspot penumbra

Dong Li[1,2], Jincheng Wang[3,2], and Yu Huang[1]

[1] *Key Laboratory of Dark Matter and Space Astronomy, Purple Mountain Observatory, CAS, Nanjing 210023, PR China*

[2] *Yunnan Key Laboratory of the Solar physics and Space Science, Kunming 650216, PR China*

[3] *Yunnan Observatories, Chinese Academy of Sciences, Kunming 650216, China*

ABSTRACT

We investigate the origin of very long-periodic pulsations (VLPs) in the white-light emission of an X6.4 flare on 2024 February 22 (SOL2024-02-22T22:08), which occurred at the edge of a sunspot group. The flare white-light fluxes reveal four successive and repetitive pulsations, which are simultaneously measured by the Helioseismic and Magnetic Imager and the White-light Solar Telescope. A quasi-period of $8.6^{+1.5}_{-1.9}$ minutes, determined by the Morlet wavelet transform, is detected in the visible continuum channel. The modulation depth, which is defined as the ratio between the oscillatory amplitude and its long-term trend, is smaller than 0.1%, implying that the QPP feature is a weak wave process. Imaging observations show that the X6.4 flare occurs near a sunspot group. Moreover, the white-light brightening is located in sunspot penumbra, and a similar quasi-period of about $8.5^{+1.6}_{-1.8}$ minutes is identified in one penumbral location of the nearest sunspot. The map of Fourier power distribution suggests that a similar periodicity is universally existing in most parts of the penumbra that is close to the penumbral-photospheric boundary. Our observations support the scenario of that the white-light QPP is probably modulated by the slow-mode magnetoacoustic gravity wave leaking from the sunspot penumbra.

Subject headings: Solar white-light flares, Solar oscillations, Sunspots

1. Introduction

The flare seen in the visible continuum is often called the white-light flare (i.e., WLF), which was first reported by Carrington (Carrington 1859). It is a rare flare event compared to the soft X-ray (SXR) flare on the Sun, mainly because of the strong optical background in the photosphere; for instance, the enhancement of the visible continuum during the WLF is typically

Correspondence should be sent to: lidong@pmo.ac.cn

5%−50% (Jess et al. 2008; Namekata et al. 2017; Li et al. 2024a). Based on the flare location in the solar surface, WLFs are classified into off-limb and on-disk flares. The off-limb WLF, with a visible continuum source detected beyond the solar limb, is only reported in a few cases (Martínez Oliveros et al. 2014; Fremstad et al. 2023). Conversely, the on-disk optical continuum brightening has been reported in the majority of the WLFs (Song & Tian 2018a; Joshi et al. 2021). It is widely known that the visible continuum emissions of WLFs are strongly correlated with the microwave and hard X-ray (HXR) emissions temporally and spatially (Krucker et al. 2015; Li et al. 2023a). Such a strong correlation may indicate that the flare white-light radiation is highly associated with electron beams that are accelerated by the flare energy (Ding et al. 2003). However, those nonthermal electrons hardly penetrate into the photosphere, where the originated source of optical continua is located (Najita & Orrall 1970). Thus, the white-light continuum emission may not be fully heated by a pure mechanism of electron beams, and some portions of the white-light enhancement might be caused by an additional source, such as the Alfvén wave or the hydrogen free-free emission (Heinzel et al. 2017; Song et al. 2023). This type of WLF appears to be easily seen in powerful flares on the Sun (Zhao et al. 2021; Li et al. 2023b), and they are also frequently observed in superflares in solar-type stars (Shibayama et al. 2013; Yan et al. 2021) since they both release a large amount of energies.

One common feature that is associated with the flare radiation is quasi-periodic pulsations (QPPs) in the time series during solar/stellar flares. A typical QPP is generally characterized by at least three successive and repeated pulsations in the time-dependent intensity curves (Zimovets et al. 2021). The time duration of each pulsation for one flare QPP is expected to be stationary, which is regarded as the period. However, the time scales for the observed pulsations are always non-stationary, termed as quasi-periods of non-stationarity QPPs (Nakariakov et al. 2019). The quasi-periods can be detected in a wide timescale ranging from subseconds through dozens of seconds to a few minutes (Tan et al. 2010; Hayes et al. 2020; Kashapova et al. 2020; Li et al. 2020a, 2021, 2023c; Shen et al. 2022; Collier et al. 2023; Karlický & Rybák 2023). The flare QPPs on the Sun are frequently observed in a broad wavelength range of radio/microwave, Hα, ultraviolet (UV), extreme ultraviolet (EUV), SXR/HXR, and even γ-rays (Nakariakov et al. 2010; Dolla et al. 2012; Tan et al. 2016; Dominique et al. 2018; Li 2022; Lörinčík et al. 2022; Zimovets et al. 2023; Millar et al. 2024; Zhou et al. 2024). However, they are rarely reported in the white-light continuum emission during solar flares, which may because WLFs are difficult to be detected (Zhao et al. 2021). On the other hand, the flare QPPs in white-light wave bands are often observed in solar-type stars, and their quasi-periods are always ultralong, i.e., >10 minutes (Pugh et al. 2016; Kolotkov et al. 2021), although some short-period QPPs are seen in stellar flares (Howard & MacGregor 2022). It appears that the reported periods are strongly dependent on the time resolution of the observed instruments, including the QPPs both in the solar and stellar flare.

The generation mechanism of flare QPPs is still under debate (Zimovets et al. 2021). Generally, the flare QPPs are directly modulated by the eigenmodes of magnetohydrodynamic (MHD) waves in magnetic loops or current sheets, such as the fast kink and sausage modes, the torsional Alfvén

mode, and the slow mode (Nakariakov & Kolotkov 2020). The flare QPPs can also be triggered by a quasi-periodic regime of magnetic reconnection, and the quasi-periodic reconnection could be either spontaneous or induced by external waves (Takasao & Shibata 2016; Karampelas et al. 2023). The idea is that the nonthermal electrons are periodically accelerated by the repetitive reconnection during solar flares, and thus it is easier to cause the flare QPP that was observed simultaneously in HXR and microwave emissions during the impulsive phase (Yuan et al. 2019; Li & Chen 2022). It seems that the flare QPPs in different categories are driven by various mechanisms, and one single mechanism cannot fully explain all existing QPPs, which may because the available observations cannot be adequate to distinguish between different mechanisms (Inglis et al. 2023).

One critical issue is to understand why QPPs in the white-light continuum are rarely observed in solar flares (Zhao et al. 2021) but are frequently found in white-light fluxes of stellar flares (Pugh et al. 2016; Kolotkov et al. 2021; Howard & MacGregor 2022); another is to unlock the generation mechanism of flare QPPs in the optical continuum (Zimovets et al. 2021). In this Letter, we investigated the flare QPP with a very long quasi-period in the white-light continuum and also attempted to reveal its driver. The Letter is organized as follows: Section 2 introduces observations and instruments, Section 3 presents the data analysis and main results, Section 4 offers some discussions, and a brief summary is given in Section 5.

2. Observations and Instruments

We analyzed the solar flare occurred in the active region of NOAA 13234 on 2024 February 22, which is located near a sunspot group. It was simultaneously measured by the space- and ground-based telescopes, that is, the Full-disk Vector MagnetoGraph (FMG; Deng et al. 2019), the Lyα Solar Telescope (LST; Feng et al. 2019), and the Hard X-ray Imager (HXI; Su et al. 2019) on aboard the Advanced Space-based Solar Observatory (ASO-S), the Atmospheric Imaging Assembly (AIA; Lemen et al. 2012) and the Helioseismic and Magnetic Imager (HMI; Schou et al. 2012) on board the Solar Dynamics Observatory (SDO), the Geostationary Operational Environmental Satellite (GOES), the Nobeyama Radio Polarimeters (NoRP), and the Expanded Owens Valley Solar Array (EOVSA).

ASO-S is a new space observatory that explores the connection between solar magnetic fields, solar flares, and coronal mass ejections, which has three payloads on board. FMG is designed to measure the full-disk photospheric magnetic field, and now it provides the local line-of-sight (LOS) magnetogram in the active region and also provides the white-light image at the same active region in the optical continuum channel near the Fe 5324 Å line. They have the same temporal cadence of about 120 s and a spatial resolution of $\sim$1.5″. LST is composed of two telescopes that see the entire solar disk, the Solar Disk Imager (SDI) captures the Lyα snapshot at 1216 Å, and the White-light Solar Telescope (WST) takes the white-light map at 3600 Å. The white-light map measured by WST has a temporal cadence of 120 s in the regular mode and changes to 1 s or 2 s in the flare mode. HXI takes the flare imaging spectroscopy in the HXR energy range of $\sim$10$-$300 keV. The

temporal cadence is 4 s in the regular mode and can reach to be 0.125 s in the burst mode. In this work, we used the LOS magnetogram measured by FMG, the WST map at 3600 Å, the HXI light curves, and a reconstructed map in the energy range of 20−50 keV.

SDO/AIA takes full-disk solar maps at multiple EUV/UV wave bands nearly simultaneously. The AIA maps in wave bands of UV 1600 Å and EUV 131 Å are analyzed, and their temporal cadences are 24 s and 12 s, respectively. SDO/HMI provides the full-disk solar magnetogram, dopplergram, and continuum filtergram. We analyzed the visible continuum images near the Fe 6173 Å line, which has a time cadence of 45 s. Both AIA and HMI maps were preprocessed by the standard procedures of "aia_prep.pro" and "hmi_prep.pro", and they have a same spatial resolution of 1.2″. The HMI vector magnetogram is also used to analyze the magnetic topology in the flare area, which has a spatial resolution of 1.0″ and a time cadence of 720 s. NoRP records full-disk solar fluxes at six microwave frequencies with a temporal cadence of 1 s. EOVSA provides the solar radio dynamic spectrum in the microwave frequency range of ∼1−18 GHz with a temporal cadence of about 1 s, and it can also measure the solar maps in the microwave channels. However, only a few maps are provided online[1], and one EOVSA map was used to show the flare profile in the microwave channel.

3. Data analysis and Results

Figure 1 (a) presents the light curves in SXR and white-light channels from 22:05 UT to 22:55 UT on 2024 February 22. The GOES flux in the SXR channel of 1−8 Å (black) suggests an X6.4-class flare, and it begins at 22:08 UT, peaks at 22:34 UT, and stops at 22:43 UT[2]. The GOES flux at 0.5−4 Å (blue) reveals a similar profile to that at 1−8 Å. Conversely, the white-light intensity curve measured by HMI in the visible continuum channel (deep pink) exhibits at least four successive pulsations during the flare, as marked by the four vertical dashed lines. Those successive pulsations have an average duration of roughly 8 minutes, which may be regarded as the flare QPP in the white-light emission. There are some successive peaks in the white-light time series (magenta) measured by WST at 3600 Å, and they appear to be consistent with those pulsations seen in the visible continuum channel, confirming the presence of white-light QPPs. We note that the time series at WST 3600 Å show some burst noises at about 22:18 UT and 22:37 UT, which may be due to the switching of the regular and burst modes, resulting in various temporal resolutions of WST. Figure 1 (b) shows the light curves in wavelengths of HXR, microwave, and EUV/UV during 22:05−22:55 UT. We cannot see the four successive pulsations in these light curves, which are different from the white-light flux profile. The HXR fluxes recorded by HXI (black and purple) appear as a series of successive pulses at a short time scale, and their amplitudes are very small. The light curves in wave bands of microwave (cyan) and UV flux (green) seem to reveal three successive pulses with a large amplitude, but their time duration is short (Li et al. 2024b). Two pulses in

[1]http://ovsa.njit.edu/fits/flares/2024/02/22/20240222223200/

[2]https://www.solarmonitor.org/?date=20240223

microwave and UV wave bands appear to match the pulsations in white-light channels, although they are not strictly the one-to-one correspondence, as indicated by two tomato vertical lines. The EUV flux at AIA 131 Å (coral) also reveals three successive pulsations, but they are later than the white-light pulsations, and their duration is much longer. Here, to avoid those saturated images, the time cadence of AIA 131 Å is chosen to be 24 s. Briefly, the white-light QPP cannot be seen in wave bands of HXR, microwave, and EUV/UV. At last, we want to state that the SXR/HXR and microwave fluxes recorded by GOES, HXI, and NoRP are all integrated over the entire Sun, while the time series in channels of white-light and EUV/UV are integrated over the flare area, dubbed the local flux.

In Figure 1 (c)−(e), we show multi-wavelength images during the X6.4 flare. Panel (c) plots the pseudo-intensity map with a field-view-of (FOV) of $\sim 210'' \times 210''$, which is derived from the HMI continuum images near the Fe 6173 Å line. Here, the white-light emission is significantly enhanced in the pseudo-intensity map (Song et al. 2018b). It can be seen that there are two patches of visible continuum enhancements in the pseudo-intensity map, and they are located at the edge of two sunspot penumbras. Double bright kernels are also seen in the white-light image captured by WST at 3600 Å. They both match two patches in the visible continuum channel, as indicated by the two magenta contours. These two patches appear to be connected by a hot loop system seen at AIA 131 Å, as shown by the coral contours. Figure 1 (d) draws the UV map at AIA 1600 Å, which reveals a main quasi-circular structure and a remote ribbon-like shape. This observation indicates that the X6.4 flare could be a circular-ribbon flare. The gold rectangle marks the flare area used to integrate the local flux in wave bands of white light and EUV/UV. The microwave emission measured by EOVSA at 2.87 GHz displays a ellipse profile shape (cyan contour), and it matches the main quasi-circular structure, further confirming the presence of a circular-ribbon flare. Two HXR sources appear in the energy range of HXI 20−50 keV, which are overlaid on the main quasi-circular profile, as indicated by the purple contours. Here, the HXR map is reconstructed by the HXI_CLEAN algorithm, utilizing the detectors from D29 to D91. The fine grids of G1 to G3 are excluded since they are not yet calibrated well (Li et al. 2023c). We can find that one HXR source appears to match a white-light patch, but the other HXR source is far away from another white-light patch. That is, the two HXR sources are not consistent with the double white-light patches. Figure 1 (e) shows the difference map observed by WST at 3600 Å, which clearly reveals two bright kernels. Here, the base difference map is plotted, so the white-light emissions can be enhanced. The blue and red contours represent the positive and negative magnetic fields measured by FMG, and the main quasi-circular structure of the X6.4 flare is mainly surrounded by positive magnetic fields.

In order to identify the quasi-period of the flare QPP, the wavelet transform with a mother function (Torrence & Compo 1998) is performed for the detrended time series in the visible continuum channel. The detrended time series is accomplished by subtracting the 10 minute running average from its raw intensity curve, and thus the long-term trend is suppressed, while the short-period QPP can be strengthened (Yuan et al. 2011; Tian et al. 2012). Figure 2 presents the Morlet

wavelet analysis results for white-light fluxes. Panel (a) shows the raw white-light fluxes in the HMI continuum (black) and WST 3600 Å (cyan) channels, as well as the long-term trend at the HMI continuum (dashed curve). Here, the raw flux has been used as normalization, i.e., $\frac{f-f_{\rm min}}{f_{\rm max}-f_{\rm min}}$, where f is the observed flux and $f_{\rm min}$ and $f_{\rm max}$ represent the minimum and maximum fluxes, respectively. The white-light flux at WST 3600 Å has been interpolated as a uniform cadence of 45 s, which is the same as that at the HMI continuum. Then, the linear Pearson correlation coefficient (cc.) of the two white-light fluxes is estimated to about 0.86, implying a high correlation between them. Therefore, only the Morlet wavelet analysis results at the HMI continuum are shown. Panel (b) plots the normalized detrended time series in the HMI continuum channel as normalization by its long-term trend. It clearly shows four successive pulsations (vertical lines), which match those in the raw light curve, confirming that the running average can only enhance the QPP feature but not change the period. The modulation depth, which is determined by the ratio between the oscillatory amplitude and its long-term trend, is about 0.05%−0.09%. Panels (c) and (d) draw the Morlet wavelet power spectrum and its global wavelet power spectrum. They are both dominated by a bulk of the power spectrum inside the 99% significance level, suggesting a dominant period with a large uncertainty. The dominant period is determined by the peak of the global wavelet power spectrum, and its uncertainty is estimated from the full width at the half of the 99% significance level, which is about $8.6^{+1.5}_{-1.9}$ minutes. We note that the 10-min running window is very close to the measured period, which might be caused by the artifact of the detrending process. Therefore, a long running window of 15 minutes is used for detrending, and the global wavelet power spectrum is shown in Figure 2 (d). The same quasi-period of about $8.6^{+1.5}_{-1.9}$ minutes is identified with the same method, as indicated by the magenta dashed curve and red dotted line. Moreover, the measured period is consistent with the average duration of the four white-light pulsations, suggesting that the white-light QPP is not a false periodicity.

In order to search for the trigger source of the white-light QPP, we perform the Fourier transform (Inglis et al. 2008; Yuan et al. 2019) on the emission intensity of every pixel in the HMI continuum channel, as shown in Figure 3. Panel (a) presents the optical continuum map measured by ASO-S/FMG near the Fe 5324 Å line, which clearly shows two groups of bright features coinciding with the two bright kernels seen in the WST 3600 Å and HMI continuum channels, as indicated by the tomato arrows. The color contours are derived from the optical continuum radiation, representing the penumbral-photospheric (cyan) and umbral-penumbral (magenta) boundaries. The hot pink line outlines a slit section that crosses the central part of the sunspot, including the umbra (i.e, magenta plus) and penumbra (i.e, green plus). Figures 3 (b) & (c) show spatial distributions of the normalized Fourier power, and they are averaged among the spectral components of 2−4 minutes and 7−9 minutes before the X6.4 flare. We note that the short-period component at 2−4 minutes is mainly located in the umbral region, and the long-period component at 7−9 minutes tends to appear in the bulk of the penumbra, especially in the surrounding area that is close to the penumbral-photospheric boundary. It is known that the Fourier power will vary with time. To trace the sources of these variations in time with the flare localization, panel (d) presents the spatial distribution of the normalized Fourier power, which is averaged among the spectral components

at 7−9 minutes during the WLF. One can immediately note that the long-period component is situated in the penumbral region. Moreover, the long-period component is especially obvious in the WLF site, as marked by the tomato arrows. This is sufficient to fix a possible link between the oscillations in the sunspot penumbra and the origin of the energy release in the WLF. Therefore, the white-light QPP is most likely to be related to the long-period component in the penumbra.

To look closely at the trigger source of the white-light QPP, we then prepare the time-distance (TD) map along a cut slit that crosses the sunspot umbra and penumbra, and the slit position is marked by a hot pink line in Figure 3 (a). The selected slit is far from the flare site, because we wanted to state that the periodicity in the sunspot is long-standing but not affected by the flare QPP. Figure 4 shows the TD maps derived from the data cube observed by HMI and AIA in the visible continuum and UV 1600 Å. Panel (a) presents the raw TD map in the HMI continuum channel, which can easily distinguish the penumbral and umbral regions, as indicated by the short green and magenta lines on the left. Then, the normalized intensity curves are extracted from the penumbral and umbral positions, as indicated by the green and magenta pluses in Figure 3. Note that the intensity curves are both averaged over 5 pixels, so that the signal-to-noise ratio is improved. We can see that the intensity curve at the penumbra reveals several large pulsations with a long time scale, while that at the umbra exhibits a number of small pulses with a short time duration. Figure 4 (b) shows the detrended TD map after removing the 10-minutes running average (Yuan et al. 2011; Tian et al. 2012) in the HMI continuum channel, which clearly shows the large pulsations at the penumbra position, where is close to the penumbral-photospheric boundary. The overplotted curve is the detrended intensity curve normalized to its long-term trend, which also shows those large pulsations with a long time scale. We note that the modulation depth is about 2%−3%, which is much bigger than that of the white-light QPP. Panel (c) plots the detrended TD map in AIA 1600 Å, and we cannot see any apparent signature of QPPs at the penumbral and umbral regions. Here, the normalized detrended intensity curve at the penumbra shows some small wiggles, but they are absolutely different from those large pulsations in the HMI continuum channel, as indicated by the overplotted curve. All these observations suggest that the long-periodic pulsations can be seen at the sunspot penumbra in the photosphere, and they cannot propagate upwardly into the chromosphere and transition region.

In order to determine the quasi-periods at the sunspot penumbra and umbra, we also perform the same wavelet transform for the detrended intensity curves in the visible continuum channel, as shown in Figure 5. Panels (a) and (b) present the Morlet wavelet power spectrum and its global wavelet power spectrum at the sunspot penumbra. They are characterized by a bulk of the power spectrum inside the 99% significance level, and a dominant period within a large uncertainty is estimated to about $8.5^{+1.6}_{-1.8}$ minutes. This quasi-period is exactly equal to that in the white-light QPP. Moreover, the quasi-period at the sunspot penumbra appears to be always present and to not only exist in the time interval of the X6.4 flare. On the other hand, panels (c) and (d) show the Morlet wavelet power spectrum and its global wavelet power spectrum at the sunspot umbra. They both reveal a quasi-period centered at about 3 minutes, which is much shorter than that at

the sunspot penumbra and white-light QPP. Similarly, the long running window of 15 minutes is also used for detrending, and their global wavelet power spectra are shown in Figure 5 (b) and (d). One can note that the quasi-period of interest is still dominated in the global power spectra, as indicated by the magenta dashed curves. The wavelet analysis results also agree with the spatial distributions of normalized Fourier power in Figure 3.

Figure 6 shows the non-potential magnetic configuration for the active region hosting the X6.4 flare derived by the nonlinear force-free field (NLFFF) extrapolation. The NLFFF extrapolation was performed by using the weighted optimization approach (Wheatland et al. 2000) with the vector magnetograms measured by SDO/HMI. Before the extrapolation, we rebinned the boundary data by 2×2 to 0.72 Mm pixel^{-1}. In this case, the extrapolation region is a box of 566×248×248 with uniform grid points, which corresponds to about 408×179×179 Mm^3. For the extrapolated magnetic field, the current-weighted average of the angle $< \theta_i >$ is smaller than 10°. It should be pointed out that the extrapolated magnetic fields satisfied both the force-free and divergence-free conditions. We note that the main quasi-circular profile and a remote ribbon-like feature seen in UV/EUV maps are overlying on a spine-fan magnetic topology, as indicated by the yellow lines, confirming the presence of the circular-ribbon flare. The two patches of white-light brightening are connected by a magnetic loop system that is rooted in the sunspot penumbra, as indicated by the blue lines. The NLFFF-extrapolated results suggest that the white-light QPP of the circular-ribbon flare should be highly associated with the penumbral oscillation in the nearby sunspot.

4. Discussions

Until now, the X6.4 flare is the second most powerful flare since the beginning of the solar cycle 25, and the Sun becomes more active than expected. The solar flare shows a significant enhancement in the white-light continuum channel, which is simultaneously observed by the ASO-S/WST in the white-light wave band of 3600 Å, the ASO-S/FMG in the optical continuum near the Fe 5324 Å line, and the SDO/HMI in the visible continuum near the Fe 6173 Å line. Thus, it could be regarded as a WLF. The WLF reveals four apparent successive pulsations with a very long period in the white-light wave band measured by HMI and WST. Next, a wavelet transform with the mother function (Torrence & Compo 1998) is used to determine the quasi-period of the white-light QPP, which is about $8.6^{+1.5}_{-1.9}$ minutes. The very long-periodic pulsations (VLPs) have been observed in wavelengths of SXR and Hα, respectively. However, those VLPs were observed in the pre-flare phase and were considered as the prediction of powerful flares (Tan et al. 2016; Li et al. 2020a). The flare QPPs with a quasi-period of roughly 8 minutes were simultaneously found in wave bands of the white-light and UV radiation at the loop-top region during an X8.2 flare, which was an off-limb WLF (Zhao et al. 2021). In our case, the VLPs can be seen from the impulsive phase to the decay phase of the X6.4 flare in the white-light wave band, and such VLPs cannot be found in wavelengths of UV and EUV. Moreover, the X6.4 flare manifested as two brightness-enhancement patches on the solar disk, regarded as an on-disk WLF, which is absolutely

different from previous observations (Tan et al. 2016; Li et al. 2020a; Zhao et al. 2021).

Fare QPPs on the Sun are frequently observed in wavelengths of SXR/HXR, UV/EUV, and radio/micowave (Dolla et al. 2012; Dominique et al. 2018; Hayes et al. 2020; Lörinčík et al. 2022; Collier et al. 2023; Karlický & Rybák 2023; Zimovets et al. 2023; Li et al. 2024c; Millar et al. 2024), and they have been reported in the Hα (Li et al. 2020a; Kashapova et al. 2020), Lyα (Li et al. 2021; Li 2022), and γ-rays (Nakariakov et al. 2010; Li & Chen 2022) emissions. However, the flare QPPs in the white-light emission, named as white-light QPPs, are rarely reported in solar flares (Zimovets et al. 2021). In this case, the white-light QPP is observed in the white-light emission at WST 3600 Å and the visible continuum radiation near the Fe 6173 Å line, but it cannot be seen in the UV emission. That is, the flare QPP with a very long period can only exist in the photosphere, and it cannot propagate upwardly into the chromosphere and transition region on the solar disk. Thus, it could be regarded as a pure white-light QPP. The modulation depth of the white-light QPP, which is identified as the ratio of the oscillating amplitude and its long-term trend, is quite small, i.e., <0.1%, indicating a weak signal of the white-light QPP. This is reasonable, because the background of the optical light radiation in the photosphere is rather strong, while the white-light enhancement of a solar flare is much weaker than the background radiation, and thus the modulation depth is very small compared to its background. This is also one reason that why the white-light QPP is rarely reported on the Sun.

It is necessary to discuss the triggered mechanism of the white-light QPP at a very long quasi-period. Generally, the flare radiation in the white-light channel is strongly associated with nonthermal electrons accelerated by the magnetic reconnection (Ding et al. 2003; Li et al. 2023a). However, the VLPs are only seen in the visible continuum channel, and they cannot be observed in wavelengths of microwave, UV/EUV, and SXR/HXR. Moreover, they can be found both in the impulsive and decay phases during the X6.4 flare. Based on these observational facts, the white-light QPP could not be triggered by the quasi-periodic regime of magnetic reconnection, which is definitely different from previous observations (Reeves et al. 2020; Zhao et al. 2021). It is well accepted that the slow wave is a weak wave process, and the white-light QPP studied here is also a weak signal. Therefore, the white-light QPP at a very long period might be modulated by the slow-mode MHD wave in the photosphere. Sych et al. (2015) have reported the possibility of flare triggering by slow-mode waves propagating from a sunspot though a selected magnetic loop to the flare site. We also note that the X6.4 flare occurs near some sunspot groups, and the white-light radiation tends to locate in the sunspot penumbra. As can be seen in the visible continuum maps measured by HMI and FMG, both the two bright patches of white-light enhancements appear in the penumbral region, which are seated in two different sunspots. Thus, we conjectured that the very-long period may be associated with the penumbral oscillation at sunspots (Loughhead & Bray 1958; Su et al. 2013; Li et al. 2020b). The very similar quasi-period of $\sim 8.5^{+1.6}_{-1.8}$ minutes is detected in the sunspot penumbral position, which is close to the penumbral-photospheric boundary and far away from the umbral-penumbral boundary. This is consistent with the previous finding that the quasi-periods of penumbral oscillations become longer and longer when they stay away from the umbra

and approach to the photosphere (Yuan 2015; Su et al. 2016; Feng et al. 2020). Similar to what has been seen in the white-light QPP, the very long pulsations at the sunspot penumbra can be only seen in the visible continuum channel. We cannot find any apparent signature of the similar quasi-period in the UV wave band of AIA 1600 Å above the sunspot penumbra. This observational feature suggests that the slow-mode MHD wave originating from the sunspot penumbra cannot penetrate into the solar upper atmosphere, such as the chromosphere, the transition region, or even the corona on the Sun. This is consistent with the theoretical expectation, that is, a magnetoacoustic cutoff frequency is always existent above the sunspot, and only the short-period wave can spread into the solar upper atmosphere (Sych et al. 2009; Sych & Nakariakov 2014; Yuan et al. 2014). Moreover, the penumbral oscillation at the very long quasi-period appears to always exist, including the time duration of nonflare and the flare eruption. Their modulation depth (such as 2%−3%) is much larger than that of the white-light QPP (i.e., <0.1%). Thus, the penumbral oscillation is basically a weak wave process, and it can influence and be a trigger for the weaker white-light QPP. At last, the two bright patches in white-light emissions are connected by magnetic loops that are rooted in sunspot penumbras, which are demonstrated by the NLFFF extrapolation. Based on those observational facts and the NLFFF-extrapolated results, we can conclude that the white-light QPP at the very long quasi-period is most likely to be modulated by a slow-mode magnetoacoustic gravity (MAG) wave that is originating from the sunspot penumbra.

5. Summary

Using the spaced-based instruments (ASO-S, GOES, and SDO), combined with the ground-based telescopes (NoRP and EOVSA) and the NLFFF extrapolation, we investigated the flare QPP and penumbral oscillation in the white-light channel. Our main conclusions are summarized as follows:

(1) The white-light QPP at a very long quasi-period is simultaneously observed by SDO/HMI and ASO-S/WST. The flare QPP is manifested as four successive VLPs in channels of the HMI visible continuum and WST 3600 Å. However, it cannot be observed in wavelengths of HXR, microwave, and UV/EUV.

(2) A quasi-period of about $8.6^{+1.5}_{-1.9}$ is detected in the visible continuum flux. Moreover, the VLPs appear in both the impulsive and decay phases, suggesting that they could not be associated with the nonthermal electrons periodically accelerated by magnetic reconnection. The modulation depth of the white-light QPP is less than 0.1%, suggesting a weak QPP signal.

(3) A quite approximate quasi-period of about $8.5^{+1.6}_{-1.8}$ minutes is observed in the sunspot penumbra in the photosphere, which is close to the penumbral-photospheric boundary. The very long quasi-period can persist for an extended period of time, but it cannot be found in the chromosphere, transition region, and corona, indicating that it hardly penetrates into the solar upper atmosphere.

(4) The white-light QPP is most likely to be modulated by the slow-mode MAG wave that is originated from the sunspot penumbra. The very long quasi-period is cut off in the photosphere, and only the short-period wave can propagate upwardly to the solar upper atmosphere.

The authors would like to thank the referee for his/her constructive comments. This work is supported by the Strategic Priority Research Program of the Chinese Academy of Sciences, grant No. XDB0560000, and the National Key R&D Program of China 2021YFA1600502 (2021YFA1600500), and 2022YFF0503002 (2022YFF0503000). D. Li is also supported by Yunnan Key Laboratory of Solar Physics and Space Science under the number YNSPCC202207. We thank the teams of ASO-S, SDO, GOES, NoRP, and EOVSA for their open data use policy. The ASO-S mission is supported by the Strategic Priority Research Program on Space Science, the Chinese Academy of Sciences, grant No. XDA15320000.

REFERENCES

Carrington, R. C. 1859, MNRAS, 20, 13.

Collier, H., Hayes, L. A., Battaglia, A. F., et al. 2023, A&A, 671, A79.

Deng, Y.-Y., Zhang, H.-Y., Yang, J.-F., et al. 2019, Research in Astronomy and Astrophysics, 19, 157.

Ding, M. D., Liu, Y., Yeh, C.-T., et al. 2003, A&A, 403, 1151.

Dolla, L., Marqué, C., Seaton, D. B., et al. 2012, ApJ, 749, L16.

Dominique, M., Zhukov, A. N., Dolla, L., et al. 2018, Sol. Phys., 293, 61.

Feng, L., Li, H., Chen, B., et al. 2019, Research in Astronomy and Astrophysics, 19, 162.

Feng, S., Deng, Z., Yuan, D., et al. 2020, Research in Astronomy and Astrophysics, 20, 117.

Fremstad, D., Guevara Gómez, J. C., Hudson, H., et al. 2023, A&A, 672, A32.

Hayes, L. A., Inglis, A. R., Christe, S., et al. 2020, ApJ, 895, 50.

Heinzel, P., Kleint, L., Kašparová, J., et al. 2017, ApJ, 847, 48.

Howard, W. S. & MacGregor, M. A. 2022, ApJ, 926, 204.

Inglis, A. R., Nakariakov, V. M., & Melnikov, V. F. 2008, A&A, 487, 1147.

Inglis, A., Hayes, L., Guidoni, S., et al. 2023, Bulletin of the American Astronomical Society, 55, 181.

Jess, D. B., Mathioudakis, M., Crockett, P. J., et al. 2008, ApJ, 688, L119.

Joshi, R., Schmieder, B., Heinzel, P., et al. 2021, A&A, 654, A31.

Karampelas, K., McLaughlin, J. A., Botha, G. J. J., et al. 2023, ApJ, 943, 131.

Karlický, M. & Rybák, J. 2023, Universe, 9, 92.

Kashapova, L. K., Kupriyanova, E. G., Xu, Z., et al. 2020, A&A, 642, A195.

Kolotkov, D. Y., Nakariakov, V. M., Holt, R., et al. 2021, ApJ, 923, L33.

Krucker, S., Saint-Hilaire, P., Hudson, H. S., et al. 2015, ApJ, 802, 19.

Lemen, J. R., Title, A. M., Akin, D. J., et al. 2012, Sol. Phys., 275, 17.

Li, D., Feng, S., Su, W., et al. 2020a, A&A, 639, L5.

Li, D., Yang, X., Bai, X. Y., et al. 2020b, A&A, 642, A231.

Li, D., Ge, M., Dominique, M., et al. 2021, ApJ, 921, 179.

Li, D. 2022, Science in China E: Technological Sciences, 65, 139.

Li, D. & Chen, W. 2022, ApJ, 931, L28.

Li, D., Li, C., Qiu, Y., et al. 2023a, ApJ, 954, 7.

Li, D., Warmuth, A., Wang, J., et al. 2023b, Research in Astronomy and Astrophysics, 23, 095017.

Li, D., Li, Z., Shi, F., et al. 2023c, A&A, 680, L15.

Li, Y., Jing, Z., Song, D.-C., et al. 2024a, ApJ, 963, L3.

Li, D., Hong, Z., Hou, Z., et al. 2024b, ApJ, 970, 77.

Li, D., Li, J., Shen, J., et al. 2024c, arXiv:2408.01179.

Loughhead, R. E. & Bray, R. J. 1958, Australian Journal of Physics, 11, 177.

Lörinčík, J., Polito, V., De Pontieu, B., et al. 2022, Frontiers in Astronomy and Space Sciences, 9, 334.

Martínez Oliveros, J.-C., Krucker, S., Hudson, H. S., et al. 2014, ApJ, 780, L28.

Millar, D. C. L., Fletcher, L., & Joshi, J. 2024, MNRAS, 527, 5916.

Nakariakov, V. M., Foullon, C., Myagkova, I. N., et al. 2010, ApJ, 708, L47.

Nakariakov, V. M., Kolotkov, D. Y., Kupriyanova, E. G., et al. 2019, Plasma Physics and Controlled Fusion, 61, 014024.

Nakariakov, V. M. & Kolotkov, D. Y. 2020, ARA&A, 58, 441.

Namekata, K., Sakaue, T., Watanabe, K., et al. 2017, ApJ, 851, 91.

Najita, K. & Orrall, F. Q. 1970, Sol. Phys., 15, 176

Pugh, C. E., Armstrong, D. J., Nakariakov, V. M., et al. 2016, MNRAS, 459, 3659.

Reeves, K. K., Polito, V., Chen, B., et al. 2020, ApJ, 905, 165.

Schou, J., Scherrer, P. H., Bush, R. I., et al. 2012, Sol. Phys., 275, 229.

Shibayama, T., Maehara, H., Notsu, S., et al. 2013, ApJS, 209, 5..

Shen, Y., Zhou, X., Duan, Y., et al. 2022, Sol. Phys., 297, 20.

Song, Y. & Tian, H. 2018a, ApJ, 867, 159.

Song, Y. L., Tian, H., Zhang, M., et al. 2018b, A&A, 613, A69.

Song, D.-C., Tian, J., Li, Y., et al. 2023, ApJ, 952, L6.

Su, J. T., Liu, Y., Liu, S., et al. 2013, ApJ, 762, 42.

Su, J. T., Ji, K. F., Banerjee, D., et al. 2016, ApJ, 816, 30.

Su, Y., Liu, W., Li, Y.-P., et al. 2019, Research in Astronomy and Astrophysics, 19, 163.

Sych, R., Nakariakov, V. M., Karlicky, M., et al. 2009, A&A, 505, 791.

Sych, R. & Nakariakov, V. M. 2014, A&A, 569, A72.

Sych, R., Karlický, M., Altyntsev, A., et al. 2015, A&A, 577, A43.

Takasao, S. & Shibata, K. 2016, ApJ, 823, 150.

Tan, B., Zhang, Y., Tan, C., et al. 2010, ApJ, 723, 25.

Tan, B., Yu, Z., Huang, J., et al. 2016, ApJ, 833, 206.

Tian, H., McIntosh, S. W., Wang, T., et al. 2012, ApJ, 759, 144.

Torrence, C. & Compo, G. P. 1998, Bulletin of the American Meteorological Society, 79, 61.

Wheatland, M. S., Sturrock, P. A., & Roumeliotis, G. 2000, ApJ, 540, 1150.

Yan, Y., He, H., Li, C., et al. 2021, MNRAS, 505, L79.

Yuan, D., Nakariakov, V. M., Chorley, N., et al. 2011, A&A, 533, A116.

Yuan, D., Sych, R., Reznikova, V. E., et al. 2014, A&A, 561, A19.

Yuan, D. 2015,Research in Astronomy and Astrophysics, 15, 1449.

Yuan, D., Feng, S., Li, D., et al. 2019, ApJ, 886, L25.

Zhao, J., Liu, W., & Vial, J.-C. 2021, ApJ, 921, L26.

Zhou, X., Shen, Y., Yuan, D., et al. 2024, Nature Communications, 15, 3281.

Zimovets, I. V., McLaughlin, J. A., Srivastava, A. K., et al. 2021, Space Sci. Rev., 217, 66.

Zimovets, I. V., Sharykin, I. N., Kaltman, T. I., et al. 2023, Geomagnetism and Aeronomy, 63, 513.

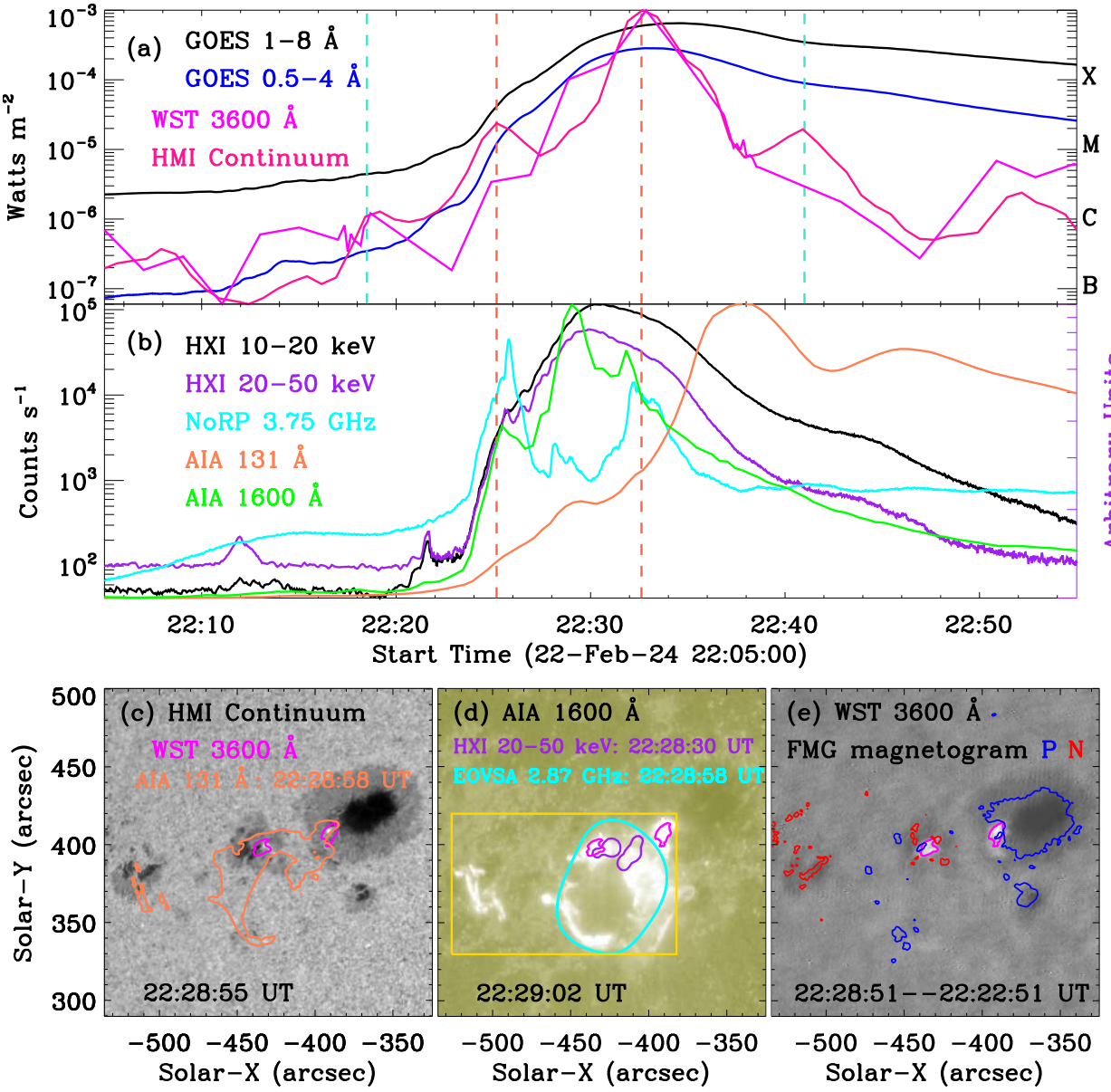

Fig. 1.— Overview of the solar flare on 2024 February 22. (a): SXR light curves recorded by GOES at 1–8 Å (black) and 0.5–4 Å (blue). White-light fluxes at WST 3600 Å (magenta), and HMI continuum (deep pink). The vertical lines (turquoise and tomato) mark four white-light peaks. (b): HXR and microwave fluxes at HXI 10–20 keV (black) and 20–50 keV (purple), and NoRP 3.75 GHz (cyan), as well as the EUV/UV fluxes at AIA 131 Å (coral) and 1600 Å (green). (c): The pseudo-intensity map with a FOV of $\sim 210'' \times 210''$ derived from the HMI continuum data. The coral contour represents the flare radiation at AIA 131 Å. (d): UV map with the same FOV at AIA 1600 Å. The purple and cyan contours outline the HXR and microwave sources at HXI 20–50 keV and EOVSA 2.87 GHz, respectively. The levels are set at 15% of their maximum. The gold rectangle marks the flare area. (e): Base difference map derived from the WST 3600 Å data. The blue and red contours represent the positive (P) and negative (N) magnetic fields at levels of ±1000 G measured by FMG. The magenta contour outlines the flare radiation at WST 3600 Å.

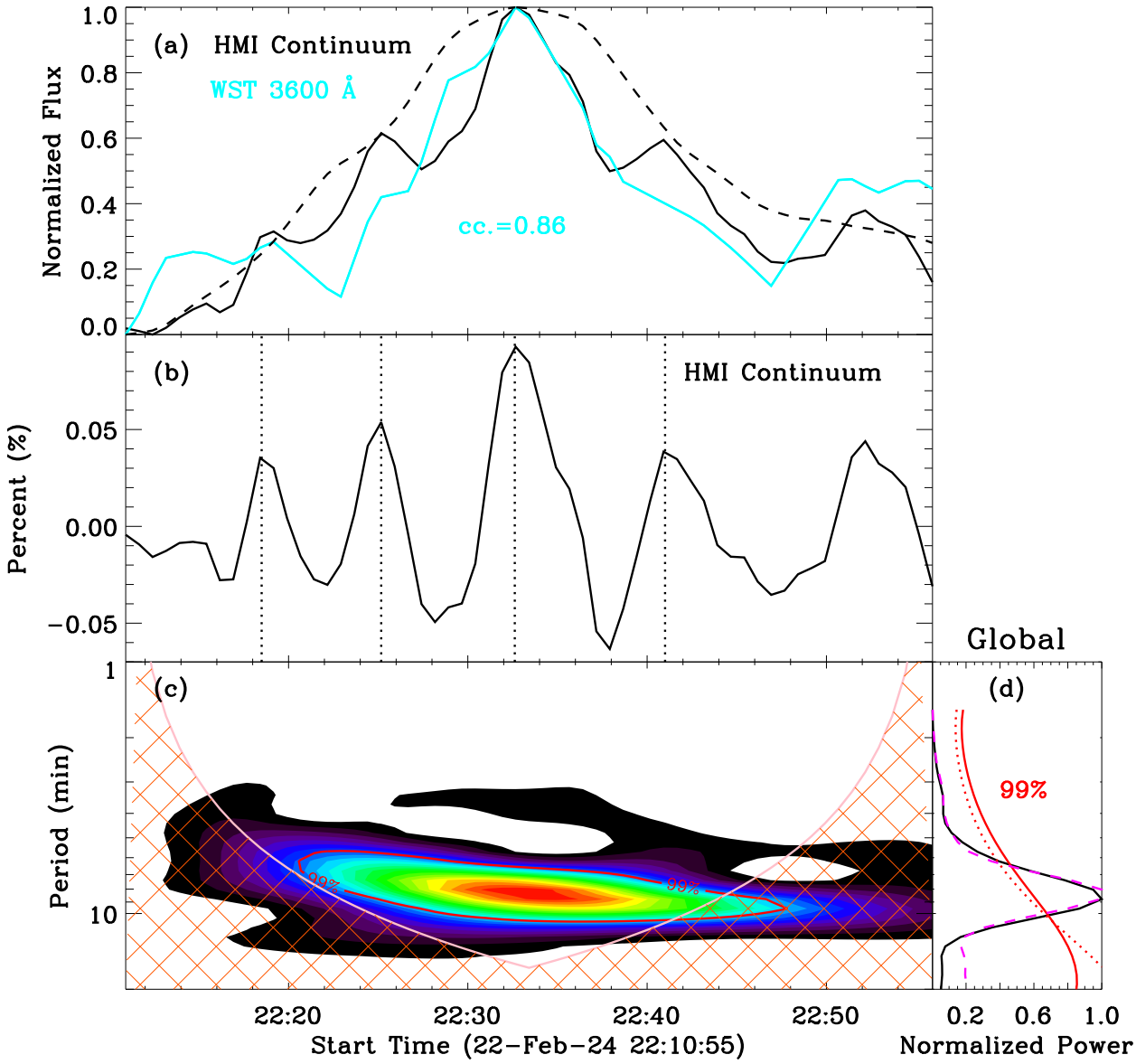

Fig. 2.— Morlet wavelet analysis results. (a): White-light fluxes measured by the HMI continuum (black) and WST 3600 Å (cyan). The overlaid dashed line represents the long-term trend at the HMI continuum. Here, the WST 3600 Å flux has been interpolated into a uniform time cadence of 45 s. (b): Detrended light curve normalized to its long-term trend at the HMI continuum. (c): Morlet wavelet power spectrum. (d): Global wavelet power spectra for the running windows of 10 minutes (black) and 15 minutes (magenta), respectively. The red contour and lines represent a significance level of 99%.

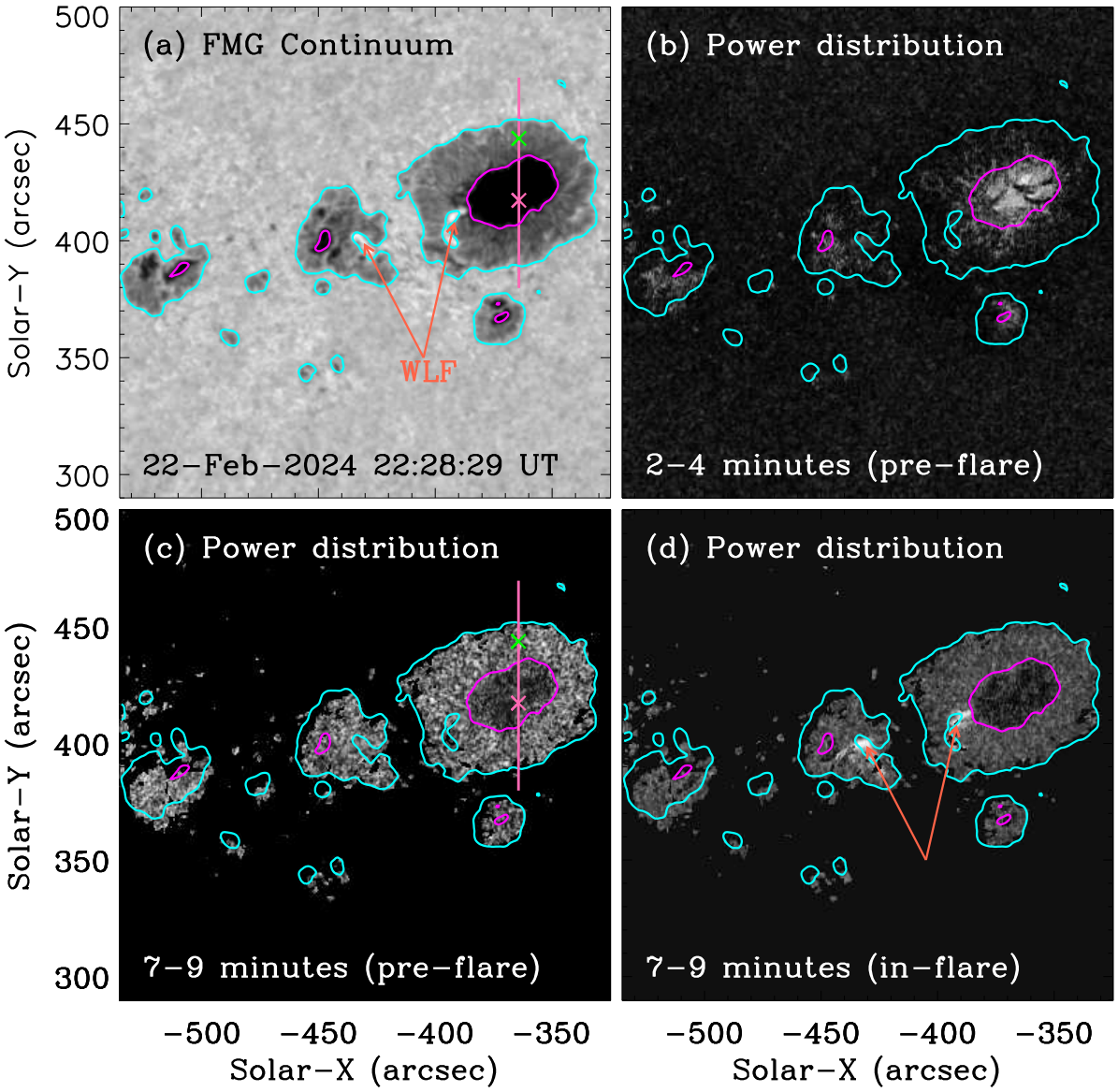

Fig. 3.— (a) The optical continuum image observed by ASO-S/FMG. The overplotted contours outline the penumbral-photospheric (cyan) and umbral-penumbral (magenta) boundaries, which are derived from the optical continuum radiation in the Fe 5324 Å line. (b) & (c) Fourier power maps that are averaged over 2-4 minutes and 7-9 minutes before the X6.4 flare. The hot pink line outline the slit position crosses the sunspot. The pluses ('+') mark the positions used to integrate the intensity curves in the penumbra (green) and umbra (hot pink). (d): Fourier power map that is averaged over 7-9 minutes during the WLF. The tomato arrows indicate the white-light brightening.

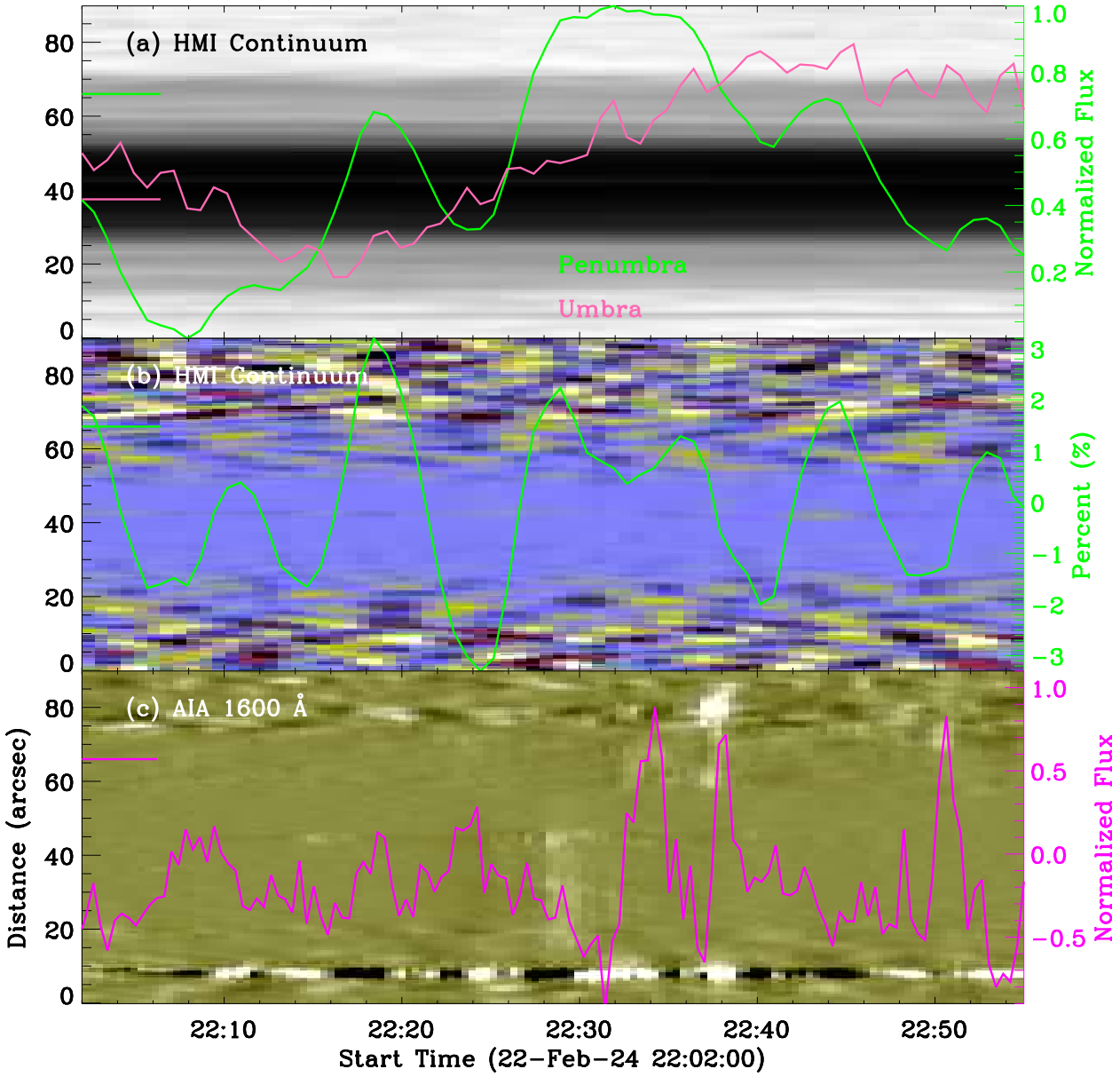

Fig. 4.— Time-distance maps along the slit (hot pink line in Figure 1) that crosses the sunspot. (a): Time-distance map at HMI continuum. (b) & (c): Time-distance maps after removing the 10-minutes running average at the HMI continuum and AIA 1600 Å. The overplotted curves are the time series that extracted at the penumbral and umbral positions, which are marked by the short lines on the left.

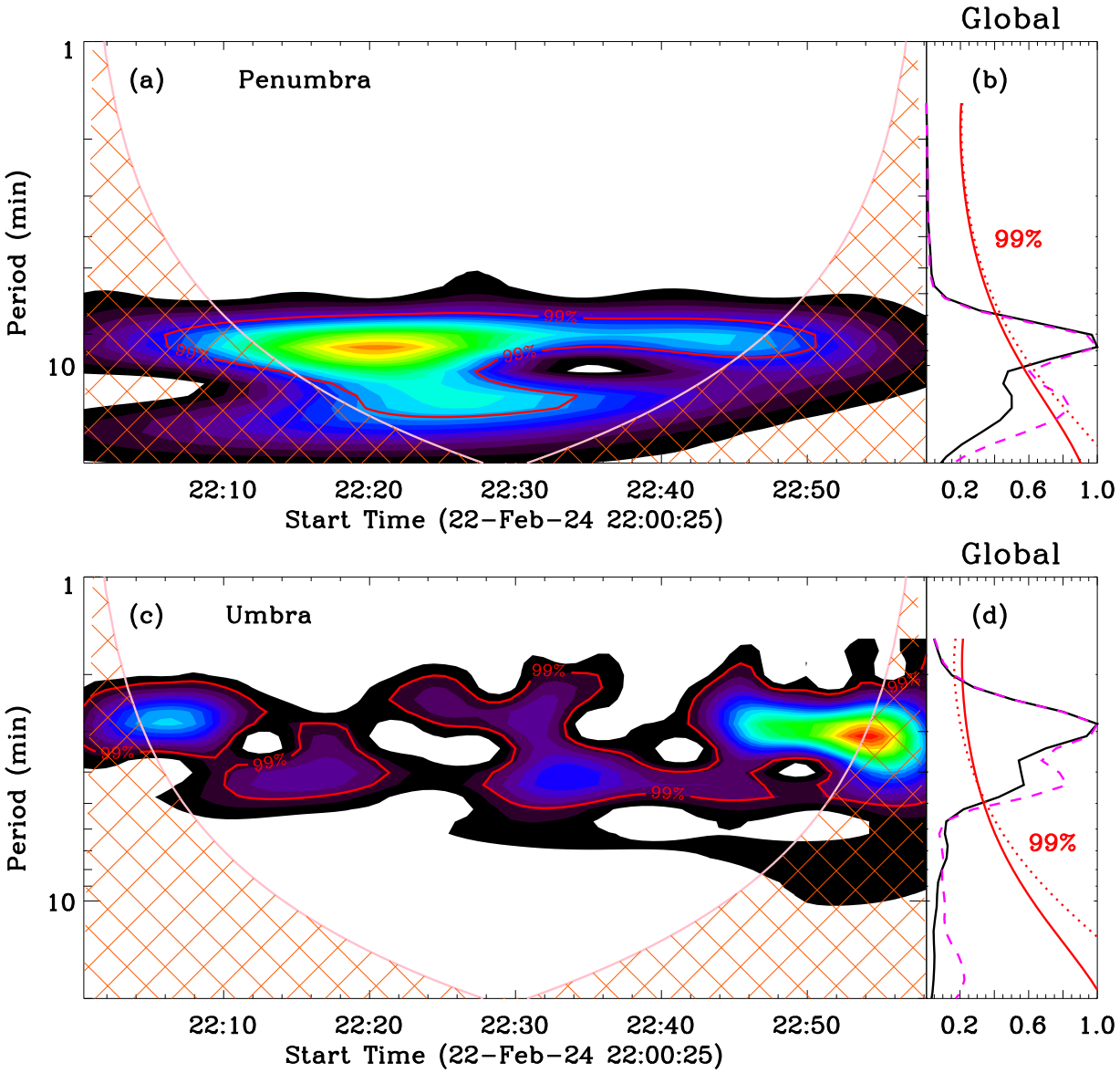

Fig. 5.— Morlet wavelet analysis results for the intensity curves at the penumbra (a & b) and umbra (c & d) of the adjacent sunspot. The black and magenta curves in panels (b) and (d) show the global wavelet power spectra for the running windows of 10 minutes and 15 minutes, respectively.

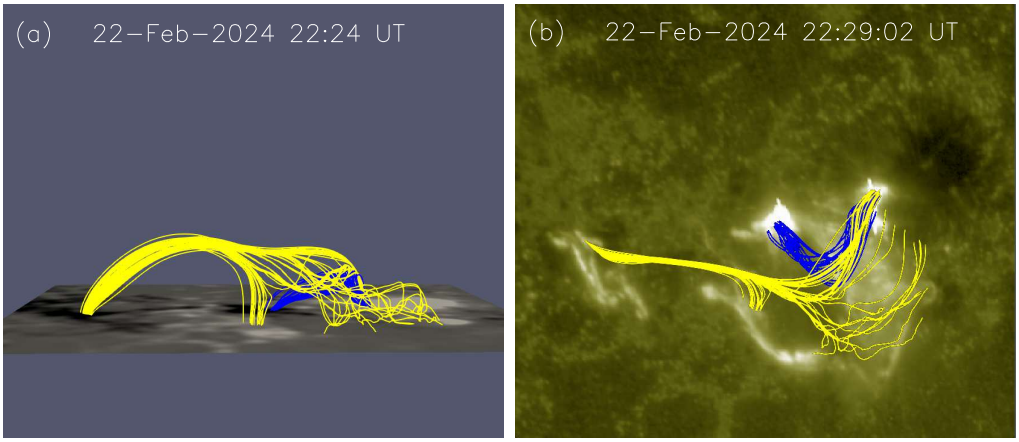

Fig. 6.— Magnetic structures derived by the NLFFF extrapolation. (a) Selected magnetic field lines overlaid on the HMI magnetogram, viewed from the front side. (b) Selected magnetic field lines overlaid on the AIA 1600 Å map, viewed from the top. The yellow lines represent a spine-fan topology, and the blue lines indicate the overlying magnetic loops.